International Journal of Fatigue 182 (2024) 108191

Contents lists available at ScienceDirect

International Journal of Fatigue

journal homepage: www.elsevier.com/locate/ijfatigue

Rapid and accurate semi-analytical method for the fatigue assessment with critical plane methods under non-proportional loading and material plasticity

M. Sgamma, A. Chiocca *, F. Frendo

Department of Civil and Industrial Engineering, University of Pisa, Pisa, Italy

ARTICLE INFO

Keywords:
Critical plane approach
Fatigue analysis
Computational cost
Speed-up calculation
Efficient method

ABSTRACT

Despite the substantial progress made over recent decades, fatigue assessment of structural components remains a challenge for designers, often culminating in unforeseen failures. Among the well established methods for evaluating fatigue, critical plane models have the capability of identifying the critical location and the direction of early crack propagation within a component. However, the use of the critical plane concept with the standard plane scanning method results extremely demanding when dealing with real-world scenarios, since, due to complex geometries, loading conditions and constraints, a comprehensive analysis of the part is required. In such situations, a more efficient computational method can be the discriminant to finalize a fatigue assessment. This study introduces a novel semi-analytical algorithm, which efficiently calculates critical plane factors. The algorithm was designed to be implemented alongside finite element analysis which may include elastic–plastic material behavior and non-proportional loading conditions. The method was tested on a notched component subjected to proportional and non-proportional loading conditions. As compared to the plane scanning method, the proposed method offers a time-efficient tool for evaluating critical plane factors and their associated plane orientations, with almost identical results.

1. Introduction

In-service fatigue loading remains a prominent cause of unexpected failures [1], making it a crucial concern for designers. While fatigue tests often depict simplified scenarios, real-world applications frequently introduce complexities such as residual stresses, stress/strain gradients, variable amplitude loading, randomness, and multiaxiality [2–8]. Particularly in such situations, finite element analysis (FEA) serves as a valuable tool for addressing these challenges [9–19]. Conventionally, solely the critical regions of a component are assessed, in order to efficiently consider stress/strain gradients, multiaxial stress and strains, and the appropriate loading histories. However, due to real-world constrains, the critical area cannot always be easily identified beforehand and assessing the complete model can be a time-consuming process which very often cannot be accomplished due to time or resource limitations. To limit this issue the designer has to select a cost-effective method for fatigue assessment, while the complexity of geometry and boundary conditions is inherent and unavoidable [20–23].

Different methods exist in order to perform fatigue assessment, including some well established in the industrial scenario and related to technical standards [24–26] and others more typically used in theoretical and applied research contexts [27–44]. In the wide range of existing methods and among local methods, those based on the critical plane concept play an important role, as they are particularly popular in both standard fatigue and fracture mechanics fields. Critical plane methods were established in the early decades of the twentieth century and have been developed and studied up to present. These methods combine a physical interpretation of the material's fracture mechanisms to define a damage parameter, associated to each possible plane orientation surrounding a point, allowing to identify the critical orientation on which the failure of the components ideally nucleates. FEA is particularly valuable for implementing these damage parameters in cases of complex loading histories and geometries. The conventional approach for calculating the critical plane factor involves scanning through all possible orientations in space for each or several nodes of the FE-model and this is typically implemented through nested *for/end* loops, resulting in substantial computational demands. The critical plane factor methodology enables the assessment of damage levels at specific critical locations within a component and to identify the direction of the early crack propagation. However, the extensive potential of such methodologies is limited due to their cumbersome implementation. As a consequence of that, in comparison to other widely-used parameters, such as nominal stress, hot spot stress, or notch stress approach,

* Corresponding author.
E-mail addresses: michele.sgamma@phd.unipi.it (M. Sgamma), andrea.chiocca@unipi.it (A. Chiocca), francesco.frendo@unipi.it (F. Frendo).

https://doi.org/10.1016/j.ijfatigue.2024.108191
Received 1 December 2023; Received in revised form 30 January 2024; Accepted 31 January 2024
Available online 2 February 2024

the critical plane method is predominantly confined to research and academia, having limited uptake in industry. The primary challenge in this computational process lies in striking the right balance between accuracy and efficiency regarding the angular increment used to scan through different planes. For this reason in most practical cases the software packages which implement such procedures use rather coarse angular increments, around 10°. However, while in several cases the error made may be negligible, there may exist instances where the result is not acceptable due to a particular combination of geometry and loading conditions.

Previous research has sought ways to reduce the computational burden required for calculating critical plane factors. Some approaches utilize analytical or semi-analytical methods to identify parameters affecting the damage factor and the directions where the damage factor is most significant. For instance, Marques et al. [45] introduced an algorithm applicable to spectral methods that enables more efficient tracking of critical plane factors or the direction of maximum stress variance. Similarly, the research conducted by Chiocca et al. [46–48], presents a range of closed-form solutions specifically developed to enhance the efficiency of critical plane models. These models encompass well-known criteria such as *Fatemi-Socie*, *Findley*, *Smith–Watson–Topper* or *Kandil–Brown–Miller*. The essence of these algorithms lies in the utilization of closed-form expressions to directly find the critical plane factor along with the corresponding critical plane orientations for every load cycle. The concept introduced by Susmel [49] allows finding the critical plane orientation of a generic load history using a reformulated concept of the maximum variance method.

Other methods aim to enhance computational speed by computing the critical plane factor solely for specific planes, eliminating the need to discretize the entire critical plane space with a fixed angular increment [50–55]. These methods involve discretizing a unit-radius sphere representing the infinite set of material plane orientations. Wentingmann et al. [56] devised an algorithm that expedites the detection of critical planes by segmenting a coarse Weber half sphere using quad elements. The effectiveness of this method depends on user-defined performance parameters, aiming to strike an optimal balance between accuracy and computational cost. Similarly, Sunde et al. [57] developed an adaptive scheme that densifies a triangular mesh around elements where the most significant damage has been observed. In certain cases, the loading condition to which the specimen is subjected to results in a reduced stress state (e.g., plane stress or plane strain) that enables a purely analytical formulation of the damage factor [58–60]. However, even when this condition is present, it is necessary to use a specific reference frame to obtain a reduced tensor configuration.

This study represent a generalization of previous works by the authors [46–48,61] and presents a novel semi-analytical method for evaluating generic critical plane (CP) parameters, for both proportional and non-proportional loading conditions under linear-elastic or elastic–plastic material behavior. The method was developed to be implemented alongside finite element simulations, accounting for a single load cycle, whether peak-to-valley or valley-to-peak. In cases of complex load histories, the method can be iteratively applied to each successive peak-to-valley and valley-to-peak pair derived from specific cycle counting formulations. The paper provides a comprehensive explanation of the methodology, starting from the theoretical background. In the second part a case study is presented under proportional and non-proportional loading conditions. A comparative analysis is carried out between the standard method of plane scanning and the methodology presented in this work in terms of solution accuracy and computational cost.

2. Critical plane factors

Even if the method is general and can be applied to different damage parameters, in the following the proposed method will illustrated with reference to two widely used critical plane factors, proposed by *Fatemi-Socie* [36] and *Findley* [37], as presented in Eq. (1) and Eq. (2), respectively

$$FS = \max\left[\frac{\Delta\gamma}{2}\left(1 + k_{FS}\frac{\sigma_{n,max}}{\sigma_y}\right)\right] \tag{1}$$

$$FI = \Delta\tau + k_{FI}\sigma_{n,max} \tag{2}$$

where $\Delta\gamma$ is the shear strain range, $\Delta\tau$ is the shear stress range, $\sigma_{n,max}$ is the maximum normal stress occurring on the plane where either $\Delta\gamma$ or $\Delta\tau$ are evaluated (depending on the CP considered) over the stress cycle, σ_y is the material yield strength, k_{FS} and k_{FI} represent material parameters. These material parameters offer insights into the respective contributions of shear stress/strain and tensile stress in the initiation mechanisms of cracks and can be obtained by comparison between the torsion fatigue limit and the push–pull fatigue limit on smooth specimens [62].

It is also worth noting that the use of Eq. (1) for the FS parameter results in a plane with a distinct orientation compared to the critical plane determined solely based on the maximum shear strain range $\Delta\gamma_{max}$ (as it is sometimes used), due to the influence of normal stress. Moreover, as already presented in [48], both the previous formulations present an analytical solutions under the assumptions of linear-elastic material behavior and proportional loading conditions. With reference to that, the present work is aimed at the proposal of a novel method for the more general conditions of non proportional loading and non linear material behavior.

2.1. Standard plane scanning method

This section will detail the typical procedure employed for calculating the CP factor using the standard plane scanning method. Upon solving a finite-element analysis (Fig. 1a), stress and strain values in various spatial directions can be computed by identifying a plane, denoted as Γ, by either its unit normal vector $\mathbf{n}$ or by two angular coordinates, θ and ψ, as illustrated in Fig. 1b. The process involves rotating the Γ plane with fixed angular increments, represented by $\Delta\theta$ and $\Delta\psi$, to calculate stress and strain values for all possible orientations. Subsequently, the plane, which maximizes the reference critical plane (CP) parameter, is identified as the critical one (Fig. 1c, showing a colored plot of the CP parameter, in which each point on the spherical surface denotes the tip of a unit vector normal to a given plane). However, the execution of this plane rotation operation necessitates the use of nested *for/end* loops, which can be computationally inefficient and labor-intensive, especially when analyzing multiple locations within a component. This procedure happens to be the one typically followed by commercial software, which employs large angular steps (i.e. about $\Delta\theta = \Delta\psi = 10°$) to optimize computation timing.

It is important to note that the accuracy of critical plane analysis typically involves a trade-off with computational expenses. When a greater number of potential planes is examined, the likelihood of identifying the point of maximum fatigue damage is enhanced. Hence, it is advisable to employ relatively fine grids, typically with angular increments ranging from 5° to 8°. These finer grids ensure that fatigue damage converges to stable values that are considered reasonably accurate [57].

In the following Section 3, for the application of this method, a rotational sequence composed of rotation ψ about the **z**-axis followed by a rotation θ about the **y**-axis in a moving reference frame will be employed as described by Eq. (3).

$$R = R_{\mathbf{z}}(\psi)R_{\mathbf{y}}(\theta) = \begin{bmatrix} \cos(\theta)\cos(\psi) & -\sin(\psi) & \cos(\psi)\sin(\theta) \\ \sin(\psi)\cos(\theta) & \cos(\psi) & \sin(\theta)\sin(\psi) \\ -\sin(\theta) & 0 & \cos(\theta) \end{bmatrix} \tag{3}$$

To perform an accurate scanning procedure, angular increments of 5° will be applied to both $\Delta\theta$ and $\Delta\psi$.

2.2. Novel semi-analytical method

Consistently with standard fatigue assessment practices, the load-time history is treated as a discrete sequence of peaks and valleys rather

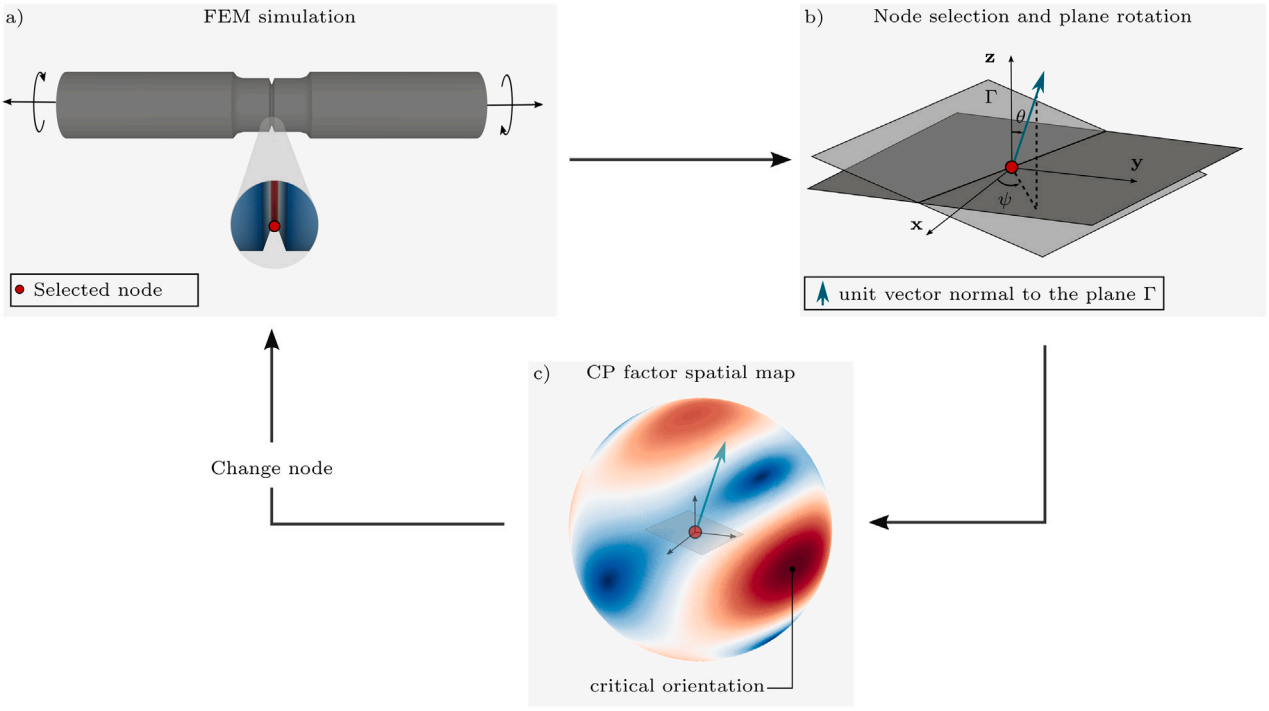

Fig. 1. Standard plane scanning sequence utilized to evaluate the critical plane factor in a selected node: (a) finite element simulation, (b) node selection and plane rotation, (c) evaluation of the critical plane factor for each rotated plane and change of the investigated node (i.e. the critical orientation identifies the spatial direction of the unit normal vector of the critical plane).

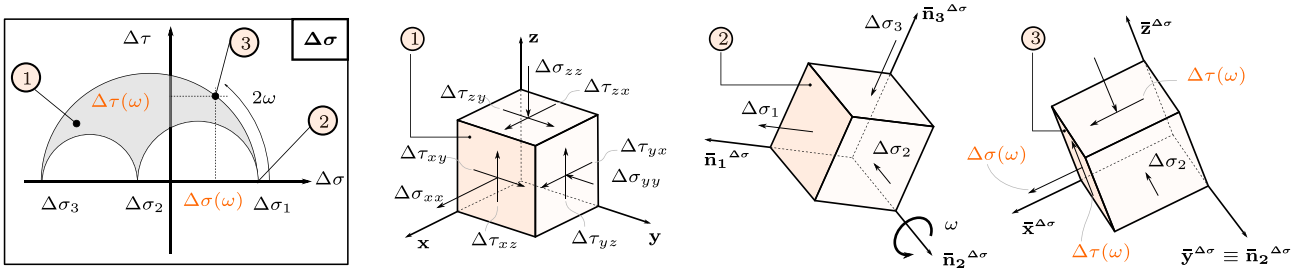

Fig. 2. Stress range tensor rotations described by means of the Mohr's circle representation and the Cauchy's infinitesimal material volume: the first configuration denotes the strain range quantities pertaining to the global reference frame, the second configuration reports the stress range components within the principal reference frame, and the third configuration present the stress range components subsequent to a ω rotation about the $\bar{\mathbf{n}}_2^{\Delta\sigma}$ axis.

than a continuous function over time. Within this framework, the stress and strain tensors $\boldsymbol{\sigma}^{(i)}$ and $\boldsymbol{\varepsilon}^{(i)}$ referring to the ith loading condition can be defined as follows:

$$\boldsymbol{\sigma}^{(i)} = \begin{bmatrix} \sigma_{xx} & \tau_{xy} & \tau_{xz} \\ & \sigma_{yy} & \tau_{yz} \\ \text{sym.} & & \sigma_{zz} \end{bmatrix}^{(i)}, \quad \boldsymbol{\varepsilon}^{(i)} = \begin{bmatrix} \varepsilon_{xx} & \frac{\gamma_{xy}}{2} & \frac{\gamma_{xz}}{2} \\ & \varepsilon_{yy} & \frac{\gamma_{yz}}{2} \\ \text{sym.} & & \varepsilon_{zz} \end{bmatrix}^{(i)} \tag{4}$$

and, during a load cycle, two successive loading conditions, are denoted as i and $i+1$. This work will not address the problem of how to find the two load steps taken for reference. Indeed, those can be derived through standard cycle counting procedures already existing in the literature such as level-crossing, peak-to-peak, simple-range, or the rainflow counting [63]. Accordingly, tensor quantities such as stress and tensor ranges can be defined, respectively as $\boldsymbol{\Delta\sigma}$ and $\boldsymbol{\Delta\varepsilon}$ as presented in Eq. (5).

$$\boldsymbol{\Delta\sigma} = \boldsymbol{\sigma}^{(i)} - \boldsymbol{\sigma}^{(i+1)}, \quad \boldsymbol{\Delta\varepsilon} = \boldsymbol{\varepsilon}^{(i)} - \boldsymbol{\varepsilon}^{(i+1)} \tag{5}$$

All the tensor quantities, including tensor differences, are defined in the same reference frame and this allows to represent them by means of matrices, a common practice adopted throughout the article.

Through an *eigenvalue-eigenvector* analysis the principal stress and strain parameters ($\Delta\sigma_1$, $\Delta\sigma_2$, $\Delta\sigma_3$), ($\sigma_1^{(i)}$, $\sigma_2^{(i)}$, $\sigma_3^{(i)}$), ($\sigma_1^{(i+1)}$, $\sigma_2^{(i+1)}$, $\sigma_3^{(i+1)}$) and ($\Delta\varepsilon_1$, $\Delta\varepsilon_2$, $\Delta\varepsilon_3$) are obtained,[1] together with the principal directions ($\bar{\mathbf{n}}_1^k$, $\bar{\mathbf{n}}_2^k$, and $\bar{\mathbf{n}}_3^k$):

$$\bar{\mathbf{n}}_1^k = \begin{bmatrix} n_{11} \\ n_{21} \\ n_{31} \end{bmatrix}^k ; \; \bar{\mathbf{n}}_2^k = \begin{bmatrix} n_{12} \\ n_{22} \\ n_{32} \end{bmatrix}^k ; \; \bar{\mathbf{n}}_3^k = \begin{bmatrix} n_{13} \\ n_{23} \\ n_{33} \end{bmatrix}^k \text{ with } k = \boldsymbol{\Delta\sigma},\ \boldsymbol{\Delta\varepsilon},\ \boldsymbol{\sigma}^{(i)},\ \boldsymbol{\sigma}^{(i+1)} \tag{6}$$

where the superscript refers to the specific tensor. These directions define the principal coordinate system. As it is well known, the rotation matrix R_p^k, which describes the rotation from the global reference frame to the principal reference frame can be defined by the direction cosines, as follows:

$$R_p^k = \begin{bmatrix} n_{11} & n_{12} & n_{13} \\ n_{21} & n_{22} & n_{23} \\ n_{31} & n_{32} & n_{33} \end{bmatrix}^k \text{ with } k = \boldsymbol{\Delta\sigma},\ \boldsymbol{\Delta\varepsilon},\ \boldsymbol{\sigma}^{(i)},\ \boldsymbol{\sigma}^{(i+1)} \tag{7}$$

[1] This holds also for the stress and for the strain range.

This transformation (from the global $Oxyz$ to the principal $O\bar{\mathbf{n}}_1^k\bar{\mathbf{n}}_2^k\bar{\mathbf{n}}_3^k$ reference frame) for the tensor $\boldsymbol{\Delta\sigma}$ is illustrated by the sequence 1–2 in Fig. 2.

For what will follow we are interested in plane orientations described by points lying on the largest circle of $\boldsymbol{\Delta\sigma}$ (as well as of $\boldsymbol{\Delta\epsilon}$, $\boldsymbol{\sigma}^{(i)}$ or $\boldsymbol{\sigma}^{(i+1)}$). Starting from the principal reference system, any point of the largest circle (i.e. moving from $\Delta\sigma_1$ to $\Delta\sigma_3$) corresponds to a plane which can be obtained by a rotation about the local $\bar{\mathbf{n}}_2$-axis. Formally, this transformation represents an intrinsic rotation of an angle ω about the $\bar{\mathbf{n}}_2$-axis of the principal reference frame, described by the rotation matrix of Eq. (8). The transition from the principal reference frame $O\bar{\mathbf{n}}_1^k\bar{\mathbf{n}}_2^k\bar{\mathbf{n}}_3^k$ to the final reference frame $O\bar{\mathbf{x}}^k\bar{\mathbf{y}}^k\bar{\mathbf{z}}^k$ is represented by means of the sequence 2–3 in Fig. 2.

$$R_{\bar{\mathbf{n}}_2} = \begin{bmatrix} \cos(\omega) & 0 & \sin(\omega) \\ 0 & 1 & 0 \\ -\sin(\omega) & 0 & \cos(\omega) \end{bmatrix} \tag{8}$$

The rotation matrix R_f^k, describing the transformation from the global to the final reference frame can then be obtained through matrices concatenation, as shown in Eq. (9).

$$R_f^k = R_p^k R_{\bar{\mathbf{n}}_2} = \begin{bmatrix} n_{11}^k\cos(\omega) - n_{31}^k\sin(\omega) & n_{12}^k & n_{11}^k\sin(\omega) + n_{31}^k\cos(\omega) \\ n_{21}^k\cos(\omega) - n_{32}^k\sin(\omega) & n_{22}^k & n_{21}^k\sin(\omega) + n_{32}^k\cos(\omega) \\ n_{31}^k\cos(\omega) - n_{33}^k\sin(\omega) & n_{23}^k & n_{31}^k\sin(\omega) + n_{33}^k\cos(\omega) \end{bmatrix} = \begin{bmatrix} R_{11} & R_{12} & R_{13} \\ R_{21} & R_{22} & R_{23} \\ R_{31} & R_{32} & R_{33} \end{bmatrix}^k \text{ with } k = \boldsymbol{\Delta\sigma},\ \boldsymbol{\Delta\epsilon},\ \boldsymbol{\sigma}^{(i)},\ \boldsymbol{\sigma}^{(i+1)} \tag{9}$$

where the $\bar{\mathbf{x}}^k$, $\bar{\mathbf{y}}^k$ and $\bar{\mathbf{z}}^k$ directions are represented by the columns (i.e. direction cosines) of R_f^k:

$$\bar{\mathbf{x}}^k = \begin{bmatrix} R_{11} \\ R_{21} \\ R_{31} \end{bmatrix}^k;\ \bar{\mathbf{y}}^k = \begin{bmatrix} R_{12} \\ R_{22} \\ R_{32} \end{bmatrix}^k;\ \bar{\mathbf{z}}^k = \begin{bmatrix} R_{13} \\ R_{23} \\ R_{33} \end{bmatrix}^k \text{ with } k = \boldsymbol{\Delta\sigma},\ \boldsymbol{\Delta\epsilon},\ \boldsymbol{\sigma}^{(i)},\ \boldsymbol{\sigma}^{(i+1)} \tag{10}$$

With reference to the critical plane concept, the maximum value of the damage parameter has to be looked for through all possible orientations. However, as previously discussed by the authors [48] for complex scenarios, including non proportional loading and material plasticity, a closed form solution is not possible. The basic idea is then to look for the local maxima that are identified along predefined paths, considering the planes which are identified by points belonging to the largest Mohr's circles, related to each of the stress and strain parameter which are involved in the damage factor, in turn.

For the FS or FI damage parameter, we have to consider three distinct parameters and the method is developed in three subsequent steps as described in the following and presented with the aid of Fig. 3a–c, t. For the sake of clarity, superscripts k will no longer be used, given the ease of identifying the tensor of reference (i.e. tensor $\boldsymbol{\Delta\sigma}$ or $\boldsymbol{\Delta\epsilon}$ in step one, tensor $\boldsymbol{\sigma}^{(i)}$ for the second step and $\boldsymbol{\sigma}^{(i+1)}$ for the third step).

1. In the first step, in order to find a local maximum of the damage factor, the plane orientations described by points lying on the largest Mohr's circle of the stress or strain range ($\boldsymbol{\Delta\sigma}$ or $\boldsymbol{\Delta\epsilon}$) are considered, according to *FI* or *FS*, respectively (Fig. 3a). During this step $\Delta\tau(\omega)$ and $\Delta\gamma(\omega)$ can be expressed in closed-form as presented in Eqs. (11)–(12), respectively.

$$\Delta\tau(\omega) = \left(\frac{\Delta\sigma_1 - \Delta\sigma_3}{2}\right)\sin(2\omega) \qquad \text{for } FI \tag{11}$$

$$\frac{\Delta\gamma}{2}(\omega) = \left(\frac{\Delta\epsilon_1 - \Delta\epsilon_3}{2}\right)\sin(2\omega) \qquad \text{for } FS \tag{12}$$

As the stress or strain range vary along the largest circle ($\boldsymbol{\Delta\epsilon}$ path in Fig. 3a), due to non-proportionality and material plasticity, the normal stress at loadstep i or loadstep $i+1$ follows a path which is included in the dashed area delimited by the three circles, determined by the principal stress components. The normal stress components acting on the plane under consideration, for both load steps i and $i+1$, can be obtained by knowing the directions $\bar{\mathbf{x}}$ and $\bar{\mathbf{z}}$ of the final reference system, relatively to $\boldsymbol{\Delta\sigma}$ or $\boldsymbol{\Delta\epsilon}$ tensors, as defined in Eq. (10).

$$\sigma^{(i)}(\omega) = \max\left[\bar{\mathbf{x}}^T\boldsymbol{\sigma}^{(i)}\bar{\mathbf{x}}, \bar{\mathbf{z}}^T\boldsymbol{\sigma}^{(i)}\bar{\mathbf{z}}\right] \tag{13}$$

$$\sigma^{(i+1)}(\omega) = \max\left[\bar{\mathbf{x}}^T\boldsymbol{\sigma}^{(i+1)}\bar{\mathbf{x}}, \bar{\mathbf{z}}^T\boldsymbol{\sigma}^{(i+1)}\bar{\mathbf{z}}\right] \tag{14}$$

It is worthnoting that the normal stresses acting on both the planes identified by the unit normal $\bar{\mathbf{x}}$ and $\bar{\mathbf{z}}$ need to be computed in order to select the maximum normal stress, since, due to the tensor symmetry, those planes are subjected to the same $\Delta\tau(\omega)$ and $\Delta\gamma(\omega)$.

Finally, the local maximum during this step is obtained starting by the values obtained along the considered path, after having fixed a discrete sequence of ω, typically in the range $[0, \frac{\pi}{4}]$.

2. During the second step, a maximization of the damage parameter, for plane orientations described by points lying on the largest circle of the stress tensor at load step i (i.e. $\boldsymbol{\sigma}^{(i)}$), is carried out (Fig. 3b). In this case, using circular representation, $\sigma^{(i)}(\omega)$ can be written in closed-form, as shown in Eq. (15).

$$\sigma^{(i)}(\omega) = \left(\frac{\sigma_1^{(i)} + \sigma_3^{(i)}}{2}\right) + \left(\frac{\sigma_1^{(i)} - \sigma_3^{(i)}}{2}\right)\cos(2\omega) \tag{15}$$

For this step, in order to evaluate all the parameters that are necessary to obtain the CP factor, it is necessary to consider the final reference system $\bar{\mathbf{x}}$, $\bar{\mathbf{y}}$ and $\bar{\mathbf{z}}$ of $\boldsymbol{\sigma}^{(i)}$ and then calculate the shear stress or shear strain range as follows:

$$\Delta\tau(\omega) = \|(\bar{\mathbf{x}}^T\boldsymbol{\Delta\sigma}\,\bar{\mathbf{y}}, \bar{\mathbf{x}}^T\boldsymbol{\Delta\sigma}\,\bar{\mathbf{z}})\| \qquad \text{for } FI \tag{16}$$

$$\frac{\Delta\gamma}{2}(\omega) = \|(\bar{\mathbf{x}}^T\boldsymbol{\Delta\epsilon}\,\bar{\mathbf{y}}, \bar{\mathbf{x}}^T\boldsymbol{\Delta\epsilon}\,\bar{\mathbf{z}})\| \qquad \text{for } FS \tag{17}$$

$$\sigma^{(i+1)}(\omega) = \bar{\mathbf{x}}^T\boldsymbol{\sigma}^{(i+1)}\bar{\mathbf{x}} \tag{18}$$

The local maximum is numerically obtained also in this step, after fixing a discretization of the ω angle, as already done in previous step.

3. Similarly to the second step, the largest circle of tensor $\boldsymbol{\sigma}^{(i+1)}$ is considered to look for a maximum of the damage parameter (Fig. 3c). In the same way as for the second step, the parameter $\sigma^{(i+1)}$ can be defined in closed form, as shown in Eq. (19).

$$\sigma^{(i+1)}(\omega) = \left(\frac{\sigma_1^{(i+1)} + \sigma_3^{(i+1)}}{2}\right) + \left(\frac{\sigma_1^{(i+1)} - \sigma_3^{(i+1)}}{2}\right)\cos(2\omega) \tag{19}$$

Then, considering the directions $\bar{\mathbf{x}}$, $\bar{\mathbf{y}}$ and $\bar{\mathbf{z}}$ related to the tensor $\boldsymbol{\sigma}^{(i+1)}$, the parameters related to tensors $\boldsymbol{\Delta\sigma}$, $\boldsymbol{\Delta\epsilon}$ and $\boldsymbol{\sigma}^{(i)}$ can be obtained as follows:

$$\Delta\tau(\omega) = \|(\bar{\mathbf{x}}^T\boldsymbol{\Delta\sigma}\,\bar{\mathbf{y}}, \bar{\mathbf{x}}^T\boldsymbol{\Delta\sigma}\,\bar{\mathbf{z}})\| \qquad \text{for } FI \tag{20}$$

$$\frac{\Delta\gamma}{2}(\omega) = \|(\bar{\mathbf{x}}^T\boldsymbol{\Delta\epsilon}\,\bar{\mathbf{y}}, \bar{\mathbf{x}}^T\boldsymbol{\Delta\epsilon}\,\bar{\mathbf{z}})\| \qquad \text{for } FS \tag{21}$$

$$\sigma^{(i)}(\omega) = \bar{\mathbf{x}}^T\boldsymbol{\sigma}^{(i)}\bar{\mathbf{x}} \tag{22}$$

Also in this case, a local maximum is finally obtained, numerically.

For each of the previous steps it is trivial to adjust the CP formulation as a function of ω:

$$FS(\omega) = \frac{\Delta\gamma}{2}(\omega)\left(1 + k_{FS}\frac{\max[\sigma^{(i)}(\omega), \sigma^{(i+1)}(\omega)]}{\sigma_y}\right) \tag{23}$$

$$FI(\omega) = \Delta\tau(\omega) + k_{FI}\max[\sigma^{(i)}(\omega), \sigma^{(i+1)}(\omega)] \tag{24}$$

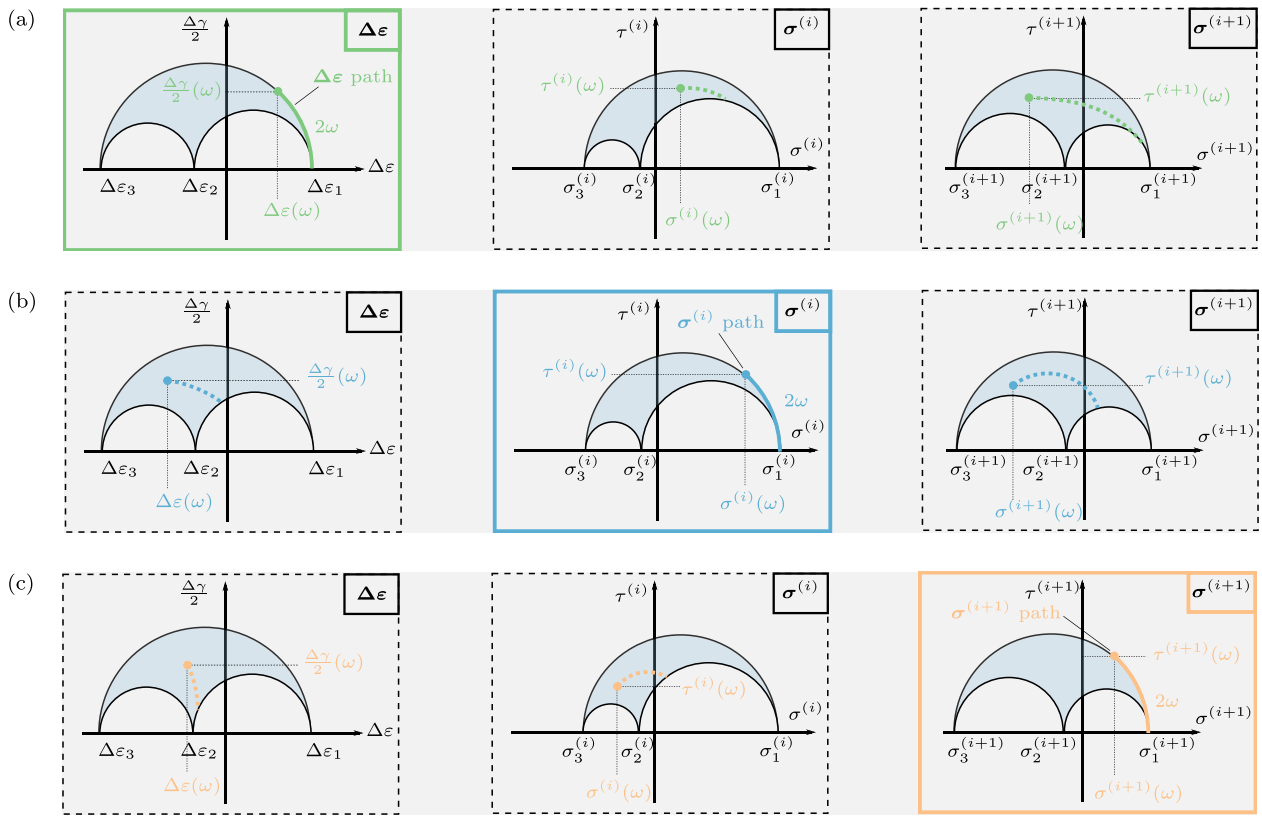

Fig. 3. Graphical representation of the semi-analytical method using Mohr's circles: paths resulting from a rotation of ω about the $\tilde{\mathbf{n}}_2^{\boldsymbol{\Delta\varepsilon}}$ axis (a), paths resulting from a rotation of ω about the $\tilde{\mathbf{n}}_2^{\boldsymbol{\sigma}^{(i)}}$ axis (b), paths resulting from a rotation of ω about the $\tilde{\mathbf{n}}_2^{\boldsymbol{\sigma}^{(i+1)}}$ axis (c).

After having obtained the local maxima of the *Fatemi-Socie* or the *Findley* damage parameter for the three cases (a), (b) and (c), independently, the critical plane factor is then defined as the maximum among the three obtained values; this is referred to as $FS(\bar{\omega})$ and $FI(\bar{\omega})$, respectively; $\bar{\omega}$ is the angle required to be used into the matrix R_f^k of Eq. (9), to obtain the orientation of the critical plane.

Starting from the expression of the rotation matrix R_f^k (Eq. (9)), the angles θ and ψ to be used to compare the solution with that obtained with the standard plane scanning method, can be obtained by using some of coefficients of the matrix expression given in Eq. (3). For example, one particular formulation of θ and ψ is the following:

$$\begin{aligned}\theta &= \arctan2(\sqrt{R_{13}^2 + R_{23}^2}, R_{33}) \\ \psi &= \arctan2(R_{23}, R_{13})\end{aligned} \tag{25}$$

To end this section, it is worth noting that, for the two critical plane factors under consideration, there are always at least two critical plane solutions. Indeed, both the critical plane models are based on shear parameters (i.e. $\Delta\gamma$ and $\Delta\tau$), for which only the absolute value is important. For this reason, it occurs that the same maximum normal stress is always associated with two opposite shear parameters, yielding at two critical planes with the same maximum CP factor, corresponding to orientations $+\omega$ and $-\omega$. This aspect has already been investigated specifically for *Fatemi-Socie* by Chiocca et al. [48]. In the numerical model, the dual solution can be implemented by rotating around $+\omega$ and $-\omega$. For this specific reason, both solutions derived from the numerical method will be referred to in the following as $FS(\pm\bar{\omega})$ and $FI(\pm\bar{\omega})$.

3. Material and methods

In order to validate the proposed method a notched specimen subjected to different combination of tension and torsion, under proportional and non-proportional loading conditions, was considered.

The technical drawing of the specimen's geometry, characterized by a notch radius of 0.2 mm, an opening angle of 30° and a minimum diameter of 16 mm, is presented in Fig. 4a. Finite Element (FE) analyses were conducted for all loading scenarios, using the 2022 version of the Ansys′ software. Specifically, 2D static structural analyses were performed, assuming small displacements. The material employed was a S355 structural steel. Elastic–plastic material behavior with kinematic hardening were employed, by means of the Chaboche model. All the material properties are presented in Table 1.

The cyclic material properties were derived experientially through a series of uniaxial tests performed on cylindrical smooth specimen made of S355JR structural steel, as described by Santus et al. [64]. An axisymmetric model with 2D structural plane elements (i.e. PLANE183) featuring 8 nodes and a quadratic shape function was used to simulate the notched specimen, as shown in Fig. 4b. The element key option was assigned a value of 6 to describe combined tensile–torsion loadings throughout 2D elements. The mesh size for the FE-model was determined through a convergence analysis, ensuring a difference smaller than 2% on the maximum von Mises stress.

The loading conditions were established by applying forces or moments along with fixed supports on the relevant model surfaces as indicated in Fig. 4b. The load sequences outlined in the Table 2 encompass one proportional loading condition (i.e. called Proportional) and two non proportional loading conditions (i.e. called Non-proportional I and Non-proportional II). Each column in Table 2 details the combination of forces or moments applied during a particular load step of the simulation ((i)-th and $(i+1)$-th load steps). Since elastic–plastic material properties were employed, a material cyclic behavior stabilization was ensured. As can be observed by the variation of the von Mises stress and the maximum shear stress along the different cycles in Fig. 5, a complete stabilization was achieved approximately after four load cycles for all the investigated load cases. For this reason, the load steps being investigated for the forthcoming analysis will be the fifth and sixth.

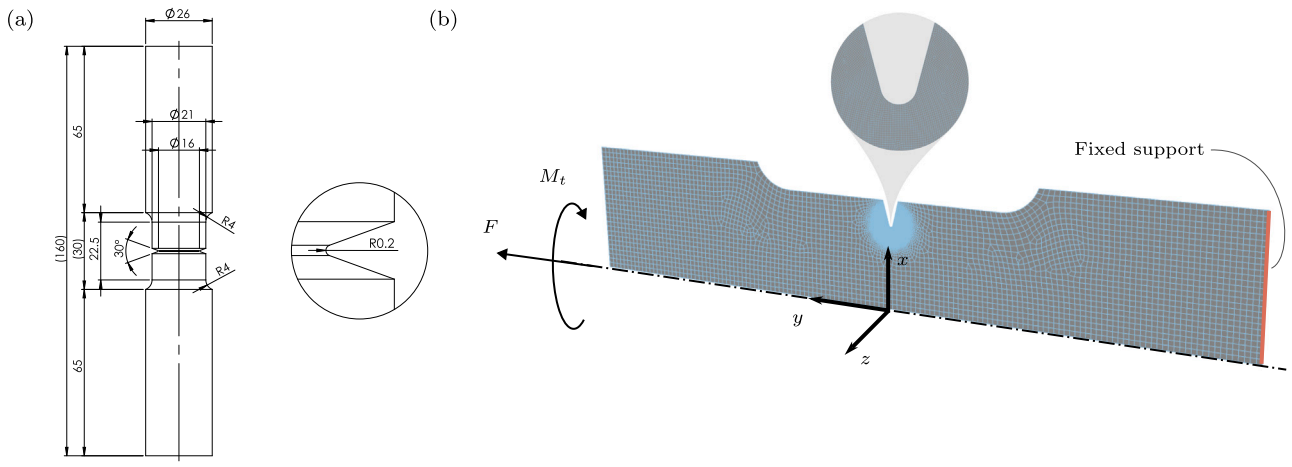

Fig. 4. Technical drawing of notched specimen (a) and finite element model including boundary conditions used during the simulation (b).

Table 1
Structural steel S355 linear-elastic and elastic–plastic material properties.

Linear-elastic						
Young's modulus E (MPa)				Poisson's ratio ν (-)		
206000				0.3		
Elastic–plastic (Chaboche kinematic hardening model)						
Yield strength σ_y (MPa)	C_1 (MPa)	γ_1	C_2 (MPa)	γ_2	C_3 (MPa)	γ_3
300	28 200	243	1.43	1	3180	0

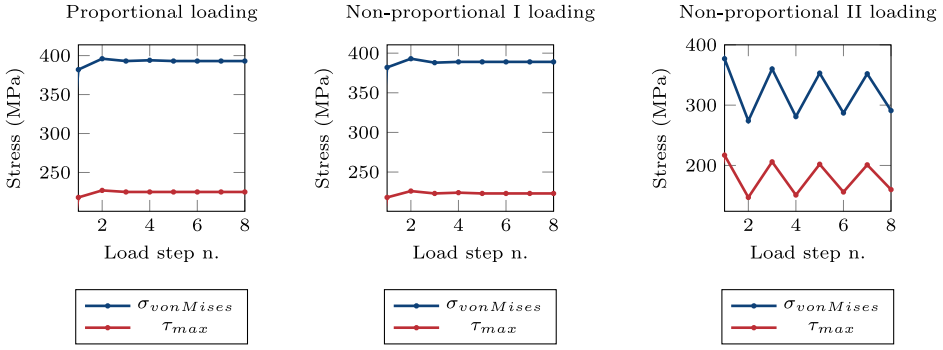

Fig. 5. Equivalent von Mises stress and maximum shear stress over eight loading cycles, for the three different loading conditions described in Table 2, showing a stabilization of the material behavior after four cycles.

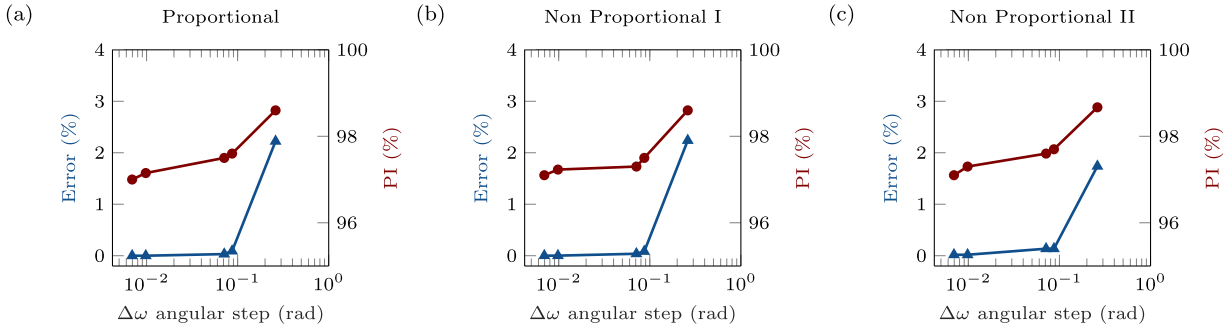

Fig. 6. Percent error (blue line) and performance index (red line) trends of FS solution when varying the angular step $\Delta\omega$ for: the Proportional loading (a), Non-proportional I loading (b) and Non-proportional II loading conditions (c).

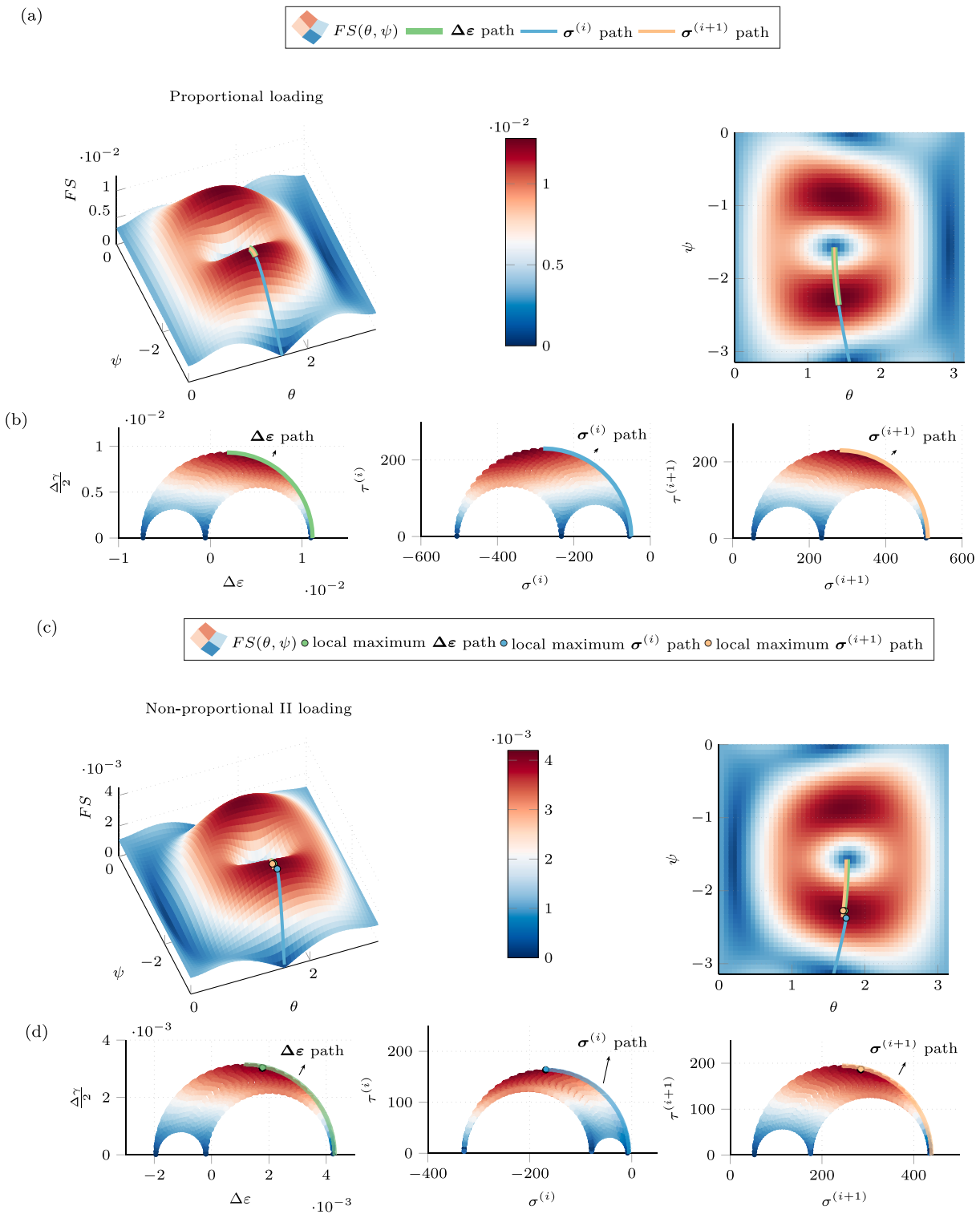

Fig. 7. Trend of FS value at the critical node of the notched specimen: comparison of the plane scanning solution and the proposed method in the Proportional loading case for $+\omega$ (a), FS solution reported on the Mohr's circles of the three reference tensors in the Proportional loading case (b), comparison of the plane scanning solution and the proposed method in the Non-proportional II loading case (c), FS solution reported on the Mohr's circles of the three reference tensors in the Non-proportional II loading case (d).

In order to calculate the critical plane factors FS and FI, a yield strength of $\sigma_y = 300\,\text{MPa}$ and material constants $k_{FS} = 0.4$, $k_{FI} = 0.67$ were utilized. The given values are within the standard range for material constants. Several studies [58,65–67] indicate how these parameters depend on the number of cycles, however for the sake of simplycity they have been kept constant. It is worth noting that, for the interested reader, the proper function $k_{FS}(N_f)$ or $k_{FI}(N_f)$ can be substituted instead of the material constants into Eqs. (23)–(24).

4. Results and discussion

In this section, the results deriving from the application of the proposed semi-analytical method are presented and discussed. The

Table 2
Force and moments combinations used during the finite element simulations.

Proportional loading			Non-proportional I loading			Non-proportional II loading		
Load step (i)	Load step ($i+1$)	Phase	Load step (i)	Load step ($i+1$)	Phase	Load step (i)	Load step ($i+1$)	Phase
F =30 kN M_t =35 N m	F =−30 kN M_t =−35 N m	0°	F =30 kN M_t =35 N m	F =−30 kN M_t =35 N m	–	F =30 kN M_t =0 kN	F =0 kN M_t =35 kN	90°

Table 3
Comparison of critical plane factors FS and FI values and orientations between the numerical method and the standard plane scanning method under proportional and non-proportional loading conditions (i.e. angles are defined in radians).

Critical plane factors comparison ($\pm\bar{\omega}$)												
	Proportional				Non-proportional I				Non-proportional II			
	Novel		Standard		Novel		Standard		Novel		Standard	
FS	0.0128		0.0128		0.0123		0.0123		0.0042		0.0042	
FI (MPa)	663		663		657		657		536		536	
θ and ψ comparison ($+\bar{\omega}$)												
	Proportional				Non-proportional I				Non-proportional II			
	Novel		Standard		Novel		Standard		Novel		Standard	
	θ	ψ	θ	ψ	θ	ψ	θ	ψ	θ	ψ	θ	ψ
FS	1.411	−2.25	1.408	−2.26	1.576	−2.25	1.578	−2.27	1.725	−2.28	1.723	−2.27
FI (MPa)	1.403	−2.19	1.407	−2.21	1.574	−2.18	1.573	−2.16	1.724	−0.945	1.735	−0.943
θ and ψ comparison ($-\bar{\omega}$)												
	Proportional				Non-proportional I				Non-proportional II			
	Novel		Standard		Novel		Standard		Novel		Standard	
	θ	ψ	θ	ψ	θ	ψ	θ	ψ	θ	ψ	θ	ψ
FS	1.41	−0.87	1.39	−0.87	1.576	−0.893	1.576	−0.891	1.725	−0.858	1.727	−0.857
FI (MPa)	1.403	−0.93	1.410	−0.92	1.574	−0.943	1.573	−0.944	1.706	−2.19	1.712	−2.17

FS and FI results deriving from the novel numerical solution are compared with those obtained through the standard plane scanning method. The mathematical framework, presented in Section 2.2, offers the prerequisite for the application of the novel methodology.

Fig. 6 shows the dramatic decrease of the relative percentage error between the proposed and standard numerical method, as the angular step of ω varies and becomes smaller that about 0.1 rad. The results refer to the three load scenarios for the FS CP factor; the same trend can be observed for the FI CP parameter, which is not reported for brevity.

In order to measure the increase in computational efficiency, the performance index (PI), defined in Eq. (26), is also reported

$$PI = \left(1 - \frac{t_{sa}}{t_{ps}}\right) \tag{26}$$

where t_{sa} denotes the computation time required by the proposed semi-analytical method, and t_{ps} denotes the computation time necessary for the standard plane scanning procedure. This index serves as a metric for assessing the computational efficiency of the proposed methodology in comparison to the standard plane scanning method. It can be noted that, while the percentage error collapses nearly to zero, the performance index slightly decrease, for the relatively larger angular steps, still exceeding 97% and this holds up to angular step of about 8.7×10^{-2}. In few words this means a huge increment in computation time, giving the possibility to develop an automated process for a comprehensive analysis (i.e. for all the nodes) of complex FE models.

The method functionality is outlined in Fig. 7a–d. The images report the FS solution derived from the plane scanning procedure ($FS(\theta, \psi)$), in the case of proportional and non-proportional II loading of Table 2. The paths obtained from the application of the three steps of the proposed method (Fig. 3), are reported together with the FS factor pattern both on the FS surface plot and on the Mohr's circles representation for the three reference tensors. In all the cases the angle ω was varied from zero to $\pi/4$. As it can be observed, for both cases, the proposed method leads to a solution which, even if it cannot be demonstrated to be exact, is very close, almost coincident, to the maximum provided by the standard plane scanning method, which requires many more mathematical computations.

In case of proportional loading, the three local maxima which are obtained by the proposed method in the three different steps are coincident, while three slightly different values are obtained in case of non proportional loading (differences below 1%).

An idea of the computation efficiency can be assumed to be provided by the points that are evaluated along a linear path (variable ω) and those that are evaluated in a surface domain (variables θ and ψ).

In addition, interestingly, it can be observed that the paths seems to follow the direction of maximum surface $FS(\theta, \psi)$ gradient; this appears to be strictly true for the proportional loading case (i.e. Fig. 7a). As a matter of fact, under proportional loading the principal reference frames of the three tensors are coincident, except for plasticity-related effects that are nonetheless quite limited. For both FS and FI, moving from $\omega = 0$ along the maximum Mohr's circle of any referenced parameter (such as $\boldsymbol{\Delta\sigma}$, $\boldsymbol{\Delta\varepsilon}$, $\boldsymbol{\sigma}^{(i)}$, or $\boldsymbol{\sigma}^{(i+1)}$) induces the most substantial increase of the shear stress or strain parameter, coupled with the least decrease among the normal stress parameters. More in details, concerning FS, if we consider moving along the maximum circle of $\boldsymbol{\Delta\varepsilon}$, starting from $\omega = 0$, then $\Delta\gamma$ experiences the greatest increase, while $\sigma_{n,max}$ undergoes the smallest decrease within the range $\omega = [0, \frac{\pi}{4}]$. Similarly, the same observations apply to $\Delta\tau$ and $\sigma_{n,max}$ in the case of FI CP factor.

Similar considerations hold for non proportional loading. In this case, as a consequence of the variation of the principal reference frame

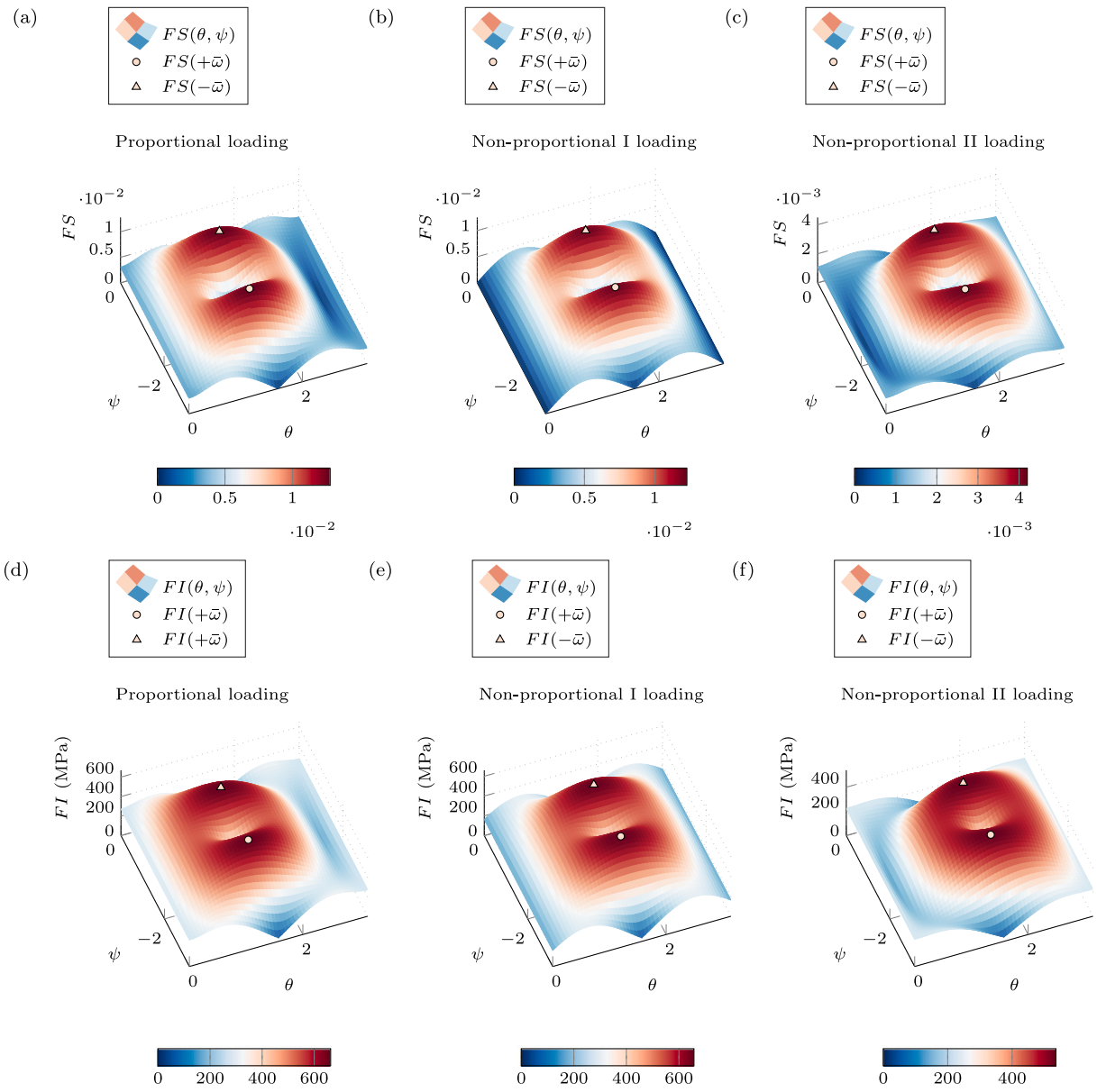

Fig. 8. Comparative analysis of CP factors solutions obtained via the standard plane scanning method ($FS(\theta,\psi)$ and $FI(\theta,\psi)$) and the proposed semi-analytical solution (FS and FI) for diverse loading conditions on a notched specimen: FS solution for proportional loading condition (a), FS solution for Non-proportional I loading condition (b), FS solution for Non-proportional II loading condition (c), FI solution for proportional loading condition (d), FI solution for Non-proportional I loading condition (e) and FI solution for Non-proportional II loading condition. The solutions provided by the semianalytical method for $+\omega$ and $-\omega$ are represented by circular and triangular white dots.

there is no guarantee of moving along the direction of maximum surface gradient. However, as it can be observed in Fig. 7c, maximizing the CP factor by using either one of the three tensor parameters, leads the solution to approach the maximum gradient direction. Also in this case the solution obtained by the proposed methodology represent a very good approximation of the maximum obtained, at the cost of many more iterations, by the standard plane scanning method; this was already demonstrated by previous analysis (Fig. 6) giving the relative error among the two methods. The critical plane factors and orientation provided by the standard plane scanning procedure and the proposed semi-analytical method are compared in Fig. 8. It is worth noting that, the semi-analytical solutions were obtained for an angular step equal to $\Delta\omega = 7.1 \times 10^{-3}$ while the angular step used for scanning through θ and ψ was set equal to 5°. Figs. 8a–c illustrate the results for the FS case, while Figs. 8d–e present the results for FI. Circular and triangular white markers represent CP orientations and values identified by the novel solution in all figures, considering both solutions obtained for $\pm\bar{\omega}$ as already discussed in Section 2.2. The semi-analytical solution aligns perfectly with the maxima derived by the plane scanning method. The $FS(\theta,\psi)$ surfaces exhibit periodicity, repeating the same pattern every π radians over both θ and ψ angular directions. Notably, the proposed solution can effectively identifies all maxima by considering the periodicity of the function $FS(\bar{\omega}+k\pi)$, with k being an integer.

To offer a comprehensive overview of the results, $FS(\bar{\omega})$ and $FI(\bar{\omega})$ values are tabulated in Table 3 for a direct methodological comparison. The table clearly shows how the solution resulting from the semi-analytical method is identical to that of the standard method except for tiny errors (< 0.5%) on the plane orientation; the errors may be due to a combination of the results numerical approximations derived from the two methods employed.

As a final consideration, it should be noted that although the computational time reduction on the single node appears minor, that on actual FE-models may be considerable.

5. Conclusions

In continuation of prior works made by the authors, a novel semi-analytical method for CP factor evaluation under more general conditions of load non proportionality and material plasticity was developed in this study. The methodology relies on stress and strain tensor invariants, employing coordinate transformation laws and was implemented using a readily available Matlab® script. In comparison with the standard plane scanning method, the basic idea of the proposed algorithm consists in looking for three local maxima, moving along predefined paths in a monodimensional domain (i.e. scan along three linear paths), instead of scanning through a bidimensional domain (i.e. scanning a surface) and this results in a extremely more efficient computation time.

Several case studies were conducted and discussed in comparison to the standard plane scanning method; multiaxial stress and strain states with elastic–plastic material behavior were utilized as case study baseline and in addition both proportional and non-proportional load cases were investigated. From the analyses and results obtained, the following conclusions can be drawn:

- the method is applicable in case of uniaxial and multiaxial proportional and non-proportional loading conditions, under linear-elastic or elastic–plastic material behavior;
- significant reduction in solution time, exceeding 97% on a single node, was observed compared to the standard plane scanning method; this reduction in computation time could enhance the feasibility of employing CP methods, particularly in the industrial context;
- the proposed method was demonstrated to furnish a solution, in terms of damage factor and plane orientation, which is practically equivalent to that obtained by the standard plane scanning method, for two of the most common critical plane factors under proportional and non proportional loading;
- the method's simplicity and reliance on fundamental tensor mathematics facilitate its implementation across various codes; its potential extension to other CP factors appears straightforward.

Reducing computation time in evaluating critical plane factors is pivotal for evaluating damage factors comprehensively, especially in complex geometries involving finite element models with a substantial node count. This speed-up enables a more exhaustive assessment of complex models under cyclic loading even under multiaxial, non-proportional and elastic–plastic assumptions. In the authors opinion this represent a significant step for a greater diffusion of critical plane methods in the scientific and industrial communities.

CRediT authorship contribution statement

M. Sgamma: Writing – review & editing, Validation, Methodology, Formal analysis, Conceptualization. **A. Chiocca:** Writing – review & editing, Writing – original draft, Visualization, Validation, Supervision, Software, Methodology, Investigation, Formal analysis, Data curation, Conceptualization. **F. Frendo:** Writing – review & editing, Validation, Supervision, Methodology, Investigation, Data curation, Conceptualization.

Declaration of competing interest

The authors declare the following financial interests/personal relationships which may be considered as potential competing interests: Andrea Chiocca reports financial support was provided by Government of Italy Ministry of Education University and Research.

Data availability

Data will be made available on request.

Acknowledgments

This paper is supported by the Ministry of University and Research (MUR) as part of the PON 2014–2020 "Research and Innovation" resources – Green Action - DM MUR 1062/2021 - Title of the Research: Sviluppo e riconversione di dispositivi automotive in ottica green: la decarbonizzazione dei veicoli e nuovi impieghi dei sistemi termo-idraulici.

Appendix. Supplementary data

A Matlab® script which implements the semi-analytical algorithm reported in the article has been uploaded to a GitHub repository: https://github.com/achiocca1/SeAn-CP.

References

[1] Bhaumik SK, Sujata M, Venkataswamy MA. Fatigue failure of aircraft components. Eng Fail Anal 2008;15(6):675–94. http://dx.doi.org/10.1016/j.engfailanal.2007.10.001.
[2] Morettini G, Braccesi C, Cianetti F, Razavi N, Solberg K, Capponi L. Collection of experimental data for multiaxial fatigue criteria verification. Fatigue Fract Eng Mater Struct 2020;43(1):162–74. http://dx.doi.org/10.1111/ffe.13101.
[3] Morettini G, Braccesi C, Cianetti F, Razavi N. Design and implementation of new experimental multiaxial random fatigue tests on Astm-A105 circular specimens. Int J Fatigue 2021;142:105983. http://dx.doi.org/10.1016/j.ijfatigue.2020.105983.
[4] Kuncham E, Sen S, Kumar P, Pathak H. An online model-based fatigue life prediction approach using extended Kalman filter. Theor Appl Fract Mech 2022;117:103143. http://dx.doi.org/10.1016/j.tafmec.2021.103143.
[5] Moda M, Chiocca A, Macoretta G, Monelli BD, Bertini L. Technological implications of the Rosenthal solution for a moving point heat source in steady state on a semi-infinite solid. Mater Des 2022;110991. http://dx.doi.org/10.1016/j.matdes.2022.110991.
[6] Chiocca A, Tamburrino F, Frendo F, Paoli A. Effects of coating on the fatigue endurance of FDM lattice structures. Proc Struct Integr 2022;42:799–805. http://dx.doi.org/10.1016/j.prostr.2022.12.101.
[7] Sgamma M, Chiocca A, Bucchi F, Frendo F. Frequency analysis of random fatigue: Setup for an experimental study. Appl Res 2023;e202200066. http://dx.doi.org/10.1002/appl.202200066.
[8] Sharma D, Hiremath SS. Compressive fatigue response of Al-Si10-Mg bionic thin tubes under constant and variable amplitude loading. Int J Fatigue 2023;168:107478. http://dx.doi.org/10.1016/j.ijfatigue.2022.107478.
[9] Frendo F, Marulo G, Chiocca A, Bertini L. Fatigue life assessment of welded joints under sequences of bending and torsion loading blocks of different lengths. Fatigue Fract Eng Mater Struct 2020;43(6):1290–304. http://dx.doi.org/10.1111/ffe.13223.
[10] Palmieri M, Zucca G, Morettini G, Landi L, Cianetti F. Vibration fatigue of FDM 3D printed structures: The use of frequency domain approach. Materials 2022;15(3):854. http://dx.doi.org/10.3390/ma15030854.
[11] Chen F, Shang D-G, Li D-H, Wang L-W. Multiaxial thermo-mechanical fatigue life prediction based on notch local stress-strain estimation considering temperature change. Eng Fract Mech 2022;265:108384. http://dx.doi.org/10.1016/j.engfracmech.2022.108384.
[12] Chiocca A, Frendo F, Bertini L. Evaluation of heat sources for the simulation of the temperature distribution in gas metal arc welded joints. Metals 2019;9(11):1142. http://dx.doi.org/10.3390/met9111142.
[13] Chiocca A, Frendo F, Bertini L. Evaluation of residual stresses in a tube-to-plate welded joint. In: MATEC web of conferences, vol. 300, EDP Sciences; 2019, p. 19005. http://dx.doi.org/10.1051/matecconf/201930019005.
[14] Chiocca A, Frendo F, Bertini L. Evaluation of residual stresses in a pipe-to-plate welded joint by means of uncoupled thermal-structural simulation and experimental tests. Int J Mech Sci 2021;199:106401. http://dx.doi.org/10.1016/j.ijmecsci.2021.106401.
[15] Chiocca A, Frendo F, Aiello F, Bertini L. Influence of residual stresses on the fatigue life of welded joints. Numerical simulation and experimental tests. Int J Fatigue 2022;162:106901. http://dx.doi.org/10.1016/j.ijfatigue.2022.106901.
[16] Meneghetti G, Campagnolo A, Visentin A, Avalle M, Benedetti M, Bighelli A, et al. Rapid evaluation of notch stress intensity factors using the peak stress method with 3D tetrahedral finite element models: Comparison of commercial codes. Fatigue Fract Eng Mater Struct 2022;45(4):1005–34. http://dx.doi.org/10.1111/ffe.13645.
[17] Tamburrino F, Chiocca A, Aruanno B, Paoli A, Lardani L, Carli E, et al. A novel digitized method for the design and additive manufacturing of orthodontic space maintainers. Appl Sci 2023;13(14):8320. http://dx.doi.org/10.3390/app13148320.

[18] Fontana F, Chiocca A, Sgamma M, Bucchi F, Frendo F. Numerical-experimental characterization of the dynamic behavior of PCB for the fatigue analysis of PCBa. Proc Struct Integr 2023;47:757–64. http://dx.doi.org/10.1016/J.PROSTR.2023.07.043.

[19] Wang WJ, Yim MS. A fatigue crack growth prediction model for cracked specimen under variable amplitude loading. Int J Fatigue 2023;168:107387. http://dx.doi.org/10.1016/j.ijfatigue.2022.107387.

[20] Alzebdeh K, Jasiuk I, Ostoja-Starzewski M. Scale and boundary conditions effects in elasticity and damage mechanics of random composites. Stud Appl Mech 1998;46(C):65–80. http://dx.doi.org/10.1016/S0922-5382(98)80035-4.

[21] Inglis HM, Geubelle PH, Matouš K. Boundary condition effects on multiscale analysis of damage localization. Phil Mag 2008;88(16):2373–97. http://dx.doi.org/10.1080/14786430802345645.

[22] Chiocca A, Frendo F, Bertini L. Experimental evaluation of relaxed strains in a pipe-to-plate welded joint by means of incremental cutting process. Procedia Struct Integr 2020;28:2157–67. http://dx.doi.org/10.1016/j.prostr.2020.11.043.

[23] Chiocca A, Frendo F, Bertini L. Residual stresses influence on the fatigue strength of structural components. Proc Struct Integr 2021;38(C):447–56. http://dx.doi.org/10.1016/j.prostr.2022.03.045.

[24] European Committee for Standardization (CEN). Eurocode 3: Design of steel structures — Part 1-9: Fatigue, 50. 2005, p. 77.

[25] Hobbacher AF. The new IIW recommendations for fatigue assessment of welded joints and components - A comprehensive code recently updated. Int J Fatigue 2009;31(1):50–8. http://dx.doi.org/10.1016/j.ijfatigue.2008.04.002.

[26] Fricke W, Gao L, Paetzold H. Fatigue assessment of local stresses at fillet welds around plate corners. Int J Fatigue 2017;101:169–76. http://dx.doi.org/10.1016/j.ijfatigue.2017.01.011.

[27] Lazzarin P, Berto F. Some expressions for the strain energy in a finite volume surrounding the root of blunt V-notches. Int J Fract 2005;135(1–4):161–85. http://dx.doi.org/10.1007/s10704-005-3943-6.

[28] Braccesi C, Morettini G, Cianetti F, Palmieri M. Evaluation of fatigue damage with an energy criterion of simple implementation. Proc Struct Integr 2018;8:192–203. http://dx.doi.org/10.1016/j.prostr.2017.12.021.

[29] Al Zamzami I, Susmel L. On the use of hot-spot stresses, effective notch stresses and the Point Method to estimate lifetime of inclined welds subjected to uniaxial fatigue loading. Int J Fatigue 2018;117:432–49. http://dx.doi.org/10.1016/j.ijfatigue.2018.08.032.

[30] Berto F, Lazzarin P. The volume-based strain energy density approach applied to static and fatigue strength assessments of notched and welded structures. Proc Eng 2009;1(1):155–8. http://dx.doi.org/10.1016/j.proeng.2009.06.036.

[31] Mroziński S. Energy-based method of fatigue damage cumulation. Int J Fatigue 2019;121:73–83. http://dx.doi.org/10.1016/j.ijfatigue.2018.12.008.

[32] Varvani-Farahani A, Haftchenari H, Panbechi M. An energy-based fatigue damage parameter for off-axis unidirectional FRP composites. Compos Struct 2007;79(3):381–9. http://dx.doi.org/10.1016/j.compstruct.2006.02.013.

[33] Karakaş, Zhang G, Sonsino CM. Critical distance approach for the fatigue strength assessment of magnesium welded joints in contrast to Neuber's effective stress method. Int J Fatigue 2018;112:21–35. http://dx.doi.org/10.1016/j.ijfatigue.2018.03.004.

[34] Taylor D, Barrett N, Lucano G. Some new methods for predicting fatigue in welded joints. Int J Fatigue 2002;24(5):509–18. http://dx.doi.org/10.1016/S0142-1123(01)00174-8.

[35] Radaj D, Sonsino CM, Fricke W. Fatigue assessment of welded joints by local approaches. second ed. 2006, p. 1–639. http://dx.doi.org/10.1533/9781845691882.

[36] Fatemi A, Socie DF. A critical plane approach to multiaxial fatigue damage including out-of-phase loading. Fatigue Fract Eng Mater Struct 1988;11(3):149–65. http://dx.doi.org/10.1111/j.1460-2695.1988.tb01169.x.

[37] Findley WN. A theory for the effect of mean stress on fatigue of metals under combined torsion and axial load or bending. J Eng Ind 1959;81(4):301–5. http://dx.doi.org/10.1115/1.4008327.

[38] Kandil FA, Brown MW, J. MK. Biaxial low-cycle fatigue failure of 316 stainless steel at elevated temperatures. In: Mechanical behaviour and nuclear applications of stainless steel at elevated temperatures. London, UK: Maney Pub; 1982.

[39] Socie D. Multiaxial fatigue damage models. J Eng Mater Technol Trans ASME 1987;109(4):293–8. http://dx.doi.org/10.1115/1.3225980.

[40] Huang J, Yang X, Shi D, Yu H, Dong C, Hu X. Systematic methodology for high temperature LCF life prediction of smooth and notched Ni-based superalloy with and without dwells. Comput Mater Sci 2014;89:65–74. http://dx.doi.org/10.1016/j.commatsci.2014.03.023.

[41] Reis L, Li B, De Freitas M. A multiaxial fatigue approach to rolling contact fatigue in railways. Int J Fatigue 2014;67:191–202. http://dx.doi.org/10.1016/j.ijfatigue.2014.02.001.

[42] Cruces AS, Lopez-Crespo P, Moreno B, Antunes FV. Multiaxial fatigue life prediction on S355 structural and offshore steel using the SKS critical plane model. Metals 2018;8(12):1060. http://dx.doi.org/10.3390/met8121060.

[43] El-sayed HM, Lotfy M, El-din Zohny HN, Riad HS. Prediction of fatigue crack initiation life in railheads using finite element analysis. Ain Shams Eng J 2018;9(4):2329–42. http://dx.doi.org/10.1016/j.asej.2017.06.003.

[44] Cruces AS, Garcia-Gonzalez A, Moreno B, Itoh T, Lopez-Crespo P. Critical plane based method for multiaxial fatigue analysis of 316 stainless steel. Theor Appl Fract Mech 2022;118:103273. http://dx.doi.org/10.1016/j.tafmec.2022.103273.

[45] Marques JME, Benasciutti D, Carpinteri A, Spagnoli A. An algorithm for fast critical plane search in computer-aided engineering durability analysis under multiaxial random loadings: Application to the Carpinteri–Spagnoli–Vantadori spectral method. Fatigue Fract Eng Mater Struct 2020;43(9):1978–93. http://dx.doi.org/10.1111/ffe.13273.

[46] Chiocca A, Frendo F, Marulo G. An efficient algorithm for critical plane factors evaluation. Int J Mech Sci 2023;242:107974. http://dx.doi.org/10.1016/j.ijmecsci.2022.107974.

[47] Chiocca A, Sgamma M, Frendo F, Bucchi F. Rapid and accurate fatigue assessment by an efficient critical plane algorithm: Application to a FSAE car rear upright. Procedia Struct Integr 2023;47:749–56. http://dx.doi.org/10.1016/J.PROSTR.2023.07.044.

[48] Chiocca A, Sgamma M, Frendo F. Closed-form solution for the Fatemi-Socie extended parameter in case of linear elasticity and proportional loading. In: Fatigue & fracture of engineering materials & structures. John Wiley & Sons, Ltd; 2023, http://dx.doi.org/10.1111/FFE.14153.

[49] Susmel L. A simple and efficient numerical algorithm to determine the orientation of the critical plane in multiaxial fatigue problems. Int J Fatigue 2010;32(11):1875–83. http://dx.doi.org/10.1016/j.ijfatigue.2010.05.004.

[50] Marulo G, Frendo F, Bertini L, Fatemi A. On the application of a critical plane approach to the life assessment of welded joints. Procedia Eng 2018;213:448–58. http://dx.doi.org/10.1016/J.PROENG.2018.02.044.

[51] Concli F, Maccioni L. Critical planes criteria applied to gear teeth: Which one is the most appropriate to characterize crack propagation? 133, 2021, p. 15–25. http://dx.doi.org/10.2495/MC210021,

[52] Behrooz. Critical plane fatigue damage analysis of a high speed microgenerator shaft. 2008, p. 1206–14.

[53] Arora P, Gupta SK, Samal MK, Chattopadhyay J. Multiaxial fatigue tests under variable strain paths and asynchronous loading and assessment of fatigue life using critical plane models. Int J Fatigue 2021;145:106049. http://dx.doi.org/10.1016/j.ijfatigue.2020.106049.

[54] Ran Y, Liu J, Xie L. Multiaxial fatigue life prediction method considering notch effect and non-proportional hardening. Eng Fail Anal 2022;136:106202. http://dx.doi.org/10.1016/j.engfailanal.2022.106202.

[55] Ran Y, Liu J, Wei Y. Probabilistic fatigue framework of notched specimens based on modified strain energy density model under multiaxial loadings. Eng Fract Mech 2022;266:108401. http://dx.doi.org/10.1016/j.engfracmech.2022.108401.

[56] Wentingmann M, Noever-Castelos P, Balzani C. An adaptive algorithm to accelerate the critical plane identification for multiaxial fatigue criteria. In: Proceedings of the 6th European conference on computational mechanics: solids, structures and coupled problems, ECCM 2018 and 7th European conference on computational fluid dynamics. 2020, p. 3745–54.

[57] Sunde SL, Berto F, Haugen B. Efficient implementation of critical plane for 3D stress histories using triangular elements. Int J Fatigue 2020;134:105448. http://dx.doi.org/10.1016/j.ijfatigue.2019.105448.

[58] Liu J, Ran Y, Wei Y, Zhang Z. A critical plane-based multiaxial fatigue life prediction method considering the material sensitivity and the shear stress. Int J Press Vessels Pip 2021;194:104532. http://dx.doi.org/10.1016/j.ijpvp.2021.104532.

[59] Albinmousa J, Al Hussain M. Polar damage sum concept for constant amplitude proportional and nonproportional multiaxial fatigue analysis. Forces Mech 2021;4:100025. http://dx.doi.org/10.1016/j.finmec.2021.100025.

[60] Ma T-H, Zhou C-Y, Gao N, Chang L, He X-H. Low cycle fatigue behavior of CP-Ti under multiaxial load-controlled mode at different multiaxial stress ratios. Int J Fatigue 2022;160:106868. http://dx.doi.org/10.1016/j.ijfatigue.2022.106868.

[61] Chiocca A, Sgamma M, Frendo F, Bucchi F, Marulo G. Fatigue assessment of a FSAE car rear upright by a closed form solution of the critical plane method. Frattura ed Integrità Strutturale 2024;18(67):153–62. http://dx.doi.org/10.3221/IGF-ESIS.67.11.

[62] Karolczuk A, Papuga J, Palin-Luc T. Progress in fatigue life calculation by implementing life-dependent material parameters in multiaxial fatigue criteria. Int J Fatigue 2020;134. http://dx.doi.org/10.1016/j.ijfatigue.2020.105509.

[63] International A. E 1049-85 - Standard practices for cycle counting in fatigue analysis. ASTM Stand 2005;85(Reapproved):1–10.

[64] Santus C, Grossi T, Romanelli L, Pedranz M, Benedetti M. A computationally fast and accurate procedure for the identification of the Chaboche isotropic-kinematic hardening model parameters based on strain-controlled cycles and asymptotic ratcheting rate. Int J Plast 2023;160:103503. http://dx.doi.org/10.1016/j.ijplas.2022.103503.

[65] McClaflin D, Fatemi A. Torsional deformation and fatigue of hardened steel including mean stress and stress gradient effects. Int J Fatigue 2004;26(7):773–84. http://dx.doi.org/10.1016/j.ijfatigue.2003.10.019.

[66] Skibicki D, Pejkowski Ł. Low-cycle multiaxial fatigue behaviour and fatigue life prediction for CuZn37 brass using the stress-strain models. Int J Fatigue 2017;102:18–36. http://dx.doi.org/10.1016/j.ijfatigue.2017.04.011.

[67] Zhu SP, Yu ZY, Correia J, De Jesus A, Berto F. Evaluation and comparison of critical plane criteria for multiaxial fatigue analysis of ductile and brittle materials. Int J Fatigue 2018;112:279–88. http://dx.doi.org/10.1016/j.ijfatigue.2018.03.028.